Supplementary Information for

Refractive Index and Thickness Measurements with Ultrahigh Sensitivity via Versatile Surface Plasmon Resonance Holographic Microscope

Lingke Wang [1,2], Jingyu Mi [1,2], Jiahao Li [1,2], Wenrui Li [1,2], Siqing Dai [1,2], Jiwei Zhang [1,2*], and Jianlin Zhao [1,2*]

[1] Key Laboratory of Light Field Manipulation and Information Acquisition, Ministry of Industry and Information Technology, and Shaanxi Key Laboratory of Optical Information Technology, Xi'an, 710129, China

[2] School of Physical Science and Technology, Northwestern Polytechnical University, Xi'an, 710129, China

[*] E-mail: jwzhang@nwpu.edu.cn; jlzhao@nwpu.edu.cn

1. Mathematical derivation of the SPR sensing principle

The underlying mechanism of SPR sensing can be rigorously modelled using the Fresnel formula,

$$r_{i,N}(\theta)=\frac{r_{i,i+1}(\theta)+r_{i+1,N}(\theta)\exp[2\mathrm{j}d_{i+1}k_{z,i+1}(\theta)]}{1+r_{i,i+1}(\theta)r_{i+1,N}(\theta)\exp[2\mathrm{j}d_{i+1}k_{z,i+1}(\theta)]}\ (\mathrm{j}=\sqrt{-1};i=1,2,...N-2) \quad (1a)$$

$$r_{i,i+1}(\theta)=\frac{\xi_{i+1}(\theta)-\xi_i(\theta)}{\xi_{i+1}(\theta)+\xi_i(\theta)}\ \ (i=1,2,...N-1) \quad (1b)$$

$$\xi_i(\theta)=\frac{\varepsilon_i}{k_{z,i}(\theta)}\ \ (i=1,2,...N) \quad (1c)$$

$$k_{z,i}(\theta)=2\pi\frac{\sqrt{\varepsilon_i-\varepsilon_1\sin^2(\theta)}}{\lambda}\ \ (i=1,2,..N) \quad (1d)$$

where i denotes the ith layer of the excitation configuration; $r_{i,i+1}$ represents the reflection coefficient at the interface between two adjacent layers; $r_{i,N}$ and $k_{z,i}$ are the complex reflection coefficient of the reflected light and wavenumber of the transmission light along the z direction in the ith layer, respectively; d_i and $\varepsilon_i = n_i^2$ are the thickness and dielectric constant of the ith layer, respectively; n_i is the corresponding RI; λ is the free-space wavelength; and θ is the angle of incidence with respect to the surface normal. The reflectivity and reflection phase shift are

$$R(\theta)=\left|r_{1,N}(\theta)\right|^2 \quad (2a)$$

$$\phi(\theta)=\arctan\left[\frac{\mathrm{Im}\,r_{1,N}(\theta)}{\mathrm{Re}\,r_{1,N}(\theta)}\right] \quad (2b)$$

Based on formulas (1) and (2), the dependence of the reflection phase shift on the dielectric thickness and RI can be established. As the phase retrieved from the double-exposure holographic recording corresponds, in principle, to the reflection phase shift difference, the dielectric thickness and RI can be effectively demodulated.

2. Phase correction operation

After dropping the mixture onto the gold film, the sample is rapidly positioned to ensure equal coverage of the sample and air regions within the CCD field of view. To minimise interference noise, the sample boundary is carefully aligned parallel to the propagation

direction of surface plasmon polaritons, indicated by the red arrow of the inset. During prolonged measurements, an additional measurement error occurs when the last-moment background hologram is used as the entire background dataset, necessitating an additional phase correction operation. Using the double-exposure method, we reconstructed phase images containing both sample and air regions. The phase correction is completed by calculating the mean phase value of the air region and subtracting it from that of the sample region.

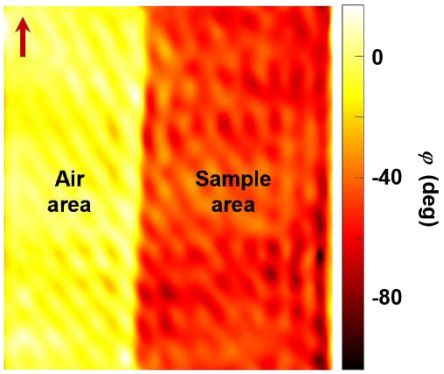

Figure S1 Additional phase correction operation.

3. Measurement results of another group of ethanol–water mixtures

A secondary concentration series of 3.5, 4.0, and 4.6 wt% was measured with 4.0 wt% as the baseline. For the 4.0 wt% mixture (initial RI = 1.3342 at 632.8 nm, interpolated from RI data for aqueous solutions in a chemical handbook), the thickness optimisation algorithm yielded a Ag–Au bilayer with thicknesses of 48 and 3 nm, respectively. The measurement results revealed a similar trend. The pure water maintained stable fluctuations around the baseline, while all φ values exhibited a significant monotonic increase over time. The optimised bilayer metal layer exhibited $\Delta\varphi$ = 6.89° versus 2.61° for the single Au layer, achieving a 2.6-fold enhancement. Similarly, a monotonic RI decrease was observed for all mass concentrations owing to the continuous volatilisation of ethanol.

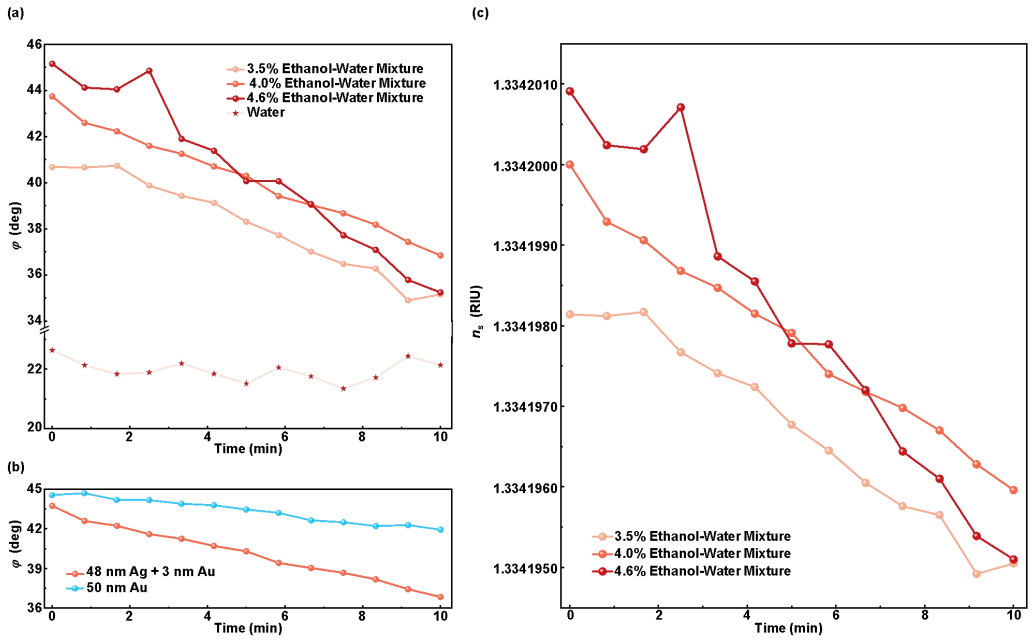

Figure S2 Measurement results of another group of ethanol–water mixtures using the microscope. a Reflection phase shift difference φ variation with time for ethanol–water mixtures with mass concentrations of 3.5, 4.0, and 4.6 wt%, and pure water. **b** Comparison of φ variations during the volatilisation of the 4.0 wt% mixture between the standard 50 nm Au and optimised Ag (48 nm)–Au (3 nm) bilayer SPR excitation configuration. The optimised Ag–Au bilayer exhibits a 2.6-fold enhancement in the variation in φ compared to that obtained by using the standard Au layer. **c** Demodulated small RI (at 632.8 nm) changes over time for ethanol–water mixtures with mass concentrations of 3.5, 4.0, and 4.6 wt%.

4. Temporal stability of a phase measurement in the SPR holographic microscope

To characterise the temporal stability of a phase measurement in the SPR holographic microscope, a long-duration holographic recording was performed without any sample, allowing a comprehensive assessment of phase measurement noise arising from environmental drift (*e.g.* mechanical vibrations and air density variations), camera readout perturbations, and laser power fluctuations. The used SPR excitation configuration comprised a bilayer of Ag (10 nm) and Au (36 nm). A sequence of holograms was recorded at a frame rate of 5 fps over 10 min, generating a total of 3000 frames. Phase distributions were then numerically reconstructed, and successive ones were subtracted to yield 2999 phase difference distributions. The temporal standard deviation was computed pixelwise across the

set of phase difference distributions. The statistical analysis of the resulting per-pixel standard deviation values yielded a histogram well fitted by a Gaussian function. The extracted phase measurement fluctuation obtained from the Gaussian fitting was 0.59°, comparable to that of conventional common-path interferometry (0.63°)[1].

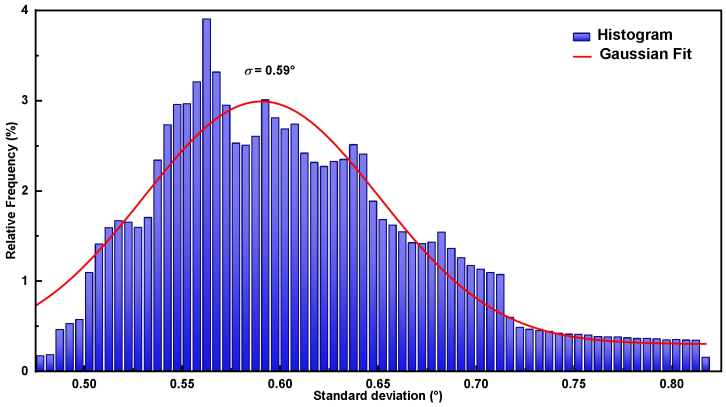

Figure S3 Histogram of the temporal standard deviation of phase difference distributions with Gaussian fitting.

5. Hologram recording principle

The bottom inset in Fig. 6a illustrates the hologram recording principle. The 45° linearly polarised light beam possesses equal horizontal and vertical components, corresponding to s- and p-polarisation states relative to the metal–dielectric interface, respectively. Upon passing through the Wollaston prism, the beam is sheared into two spatially separated components propagating at a divergence angle. The p-polarised component is capable of exciting SPR and encodes information about the dielectric properties of the object; thus, it serves as an object beam. Conversely, the s-polarised component, which remains unaffected by SPR, acts as a reference beam. Both beams subsequently pass through a polariser, which projects them onto a common linear polarisation state. This enables a coherent interference in their overlapping region, generating the off-axis hologram.

6. Composition and functionality of modules in the SPR holographic microscope

Beam Shaping and Control Module: This module integrates the fibre, negative lens, collimation lens, focusing lens, and polariser 1 within a cage system, ensuring a rigid coaxiality tolerance. The entire assembly is mounted atop a high-precision motorised vertical

translation stage via support frames. A calibrated relationship between the stage displacement and resultant beam incidence angle enables a rapid and precise angular adjustment via a motion control software.

SPR Excitation Module: This core module comprises the high-numerical-aperture microscope objective (MO), sample holder, and three-axis positioning stage. The sample holder incorporates fixed mating elements to fit with the three-axis positioning stage, which features XYZ micrometre drives for manual fine positioning of the sample region of interest.

Imaging Module: This module consists of the BS and TL positioned downstream. Critical components (MO, BS) are secured in three-axis kinematic mounts for a precise optical axis alignment. The MO, BS, and TL are rigidly attached to the microscope body with fixed arms incorporating precisely centred through-openings.

Hologram Recording Module: This final module includes a reflector, Wollaston prism, polariser 2, and CCD camera.

7. Assembly of the SPR holographic microscope

The key features of the microscope prototype include (1) the optical cage structure with a modular framework, notably miniaturising the microscope while ensuring a high degree of coaxiality and largely streamlining prealignment procedures; (2) strategic antivibration tables decoupling critical components from environmental perturbations, enhancing vibration immunity; (3) hermetically sealed housing enabling operation in regular environments, expanding deployment beyond specialised laboratories; and (4) integrated motorised stage offering programmable incidence angle scanning. Thus, the microscope is flexible to collect data at various incidence angles, which are highly valuable in SPR quantitative imaging and sensing.

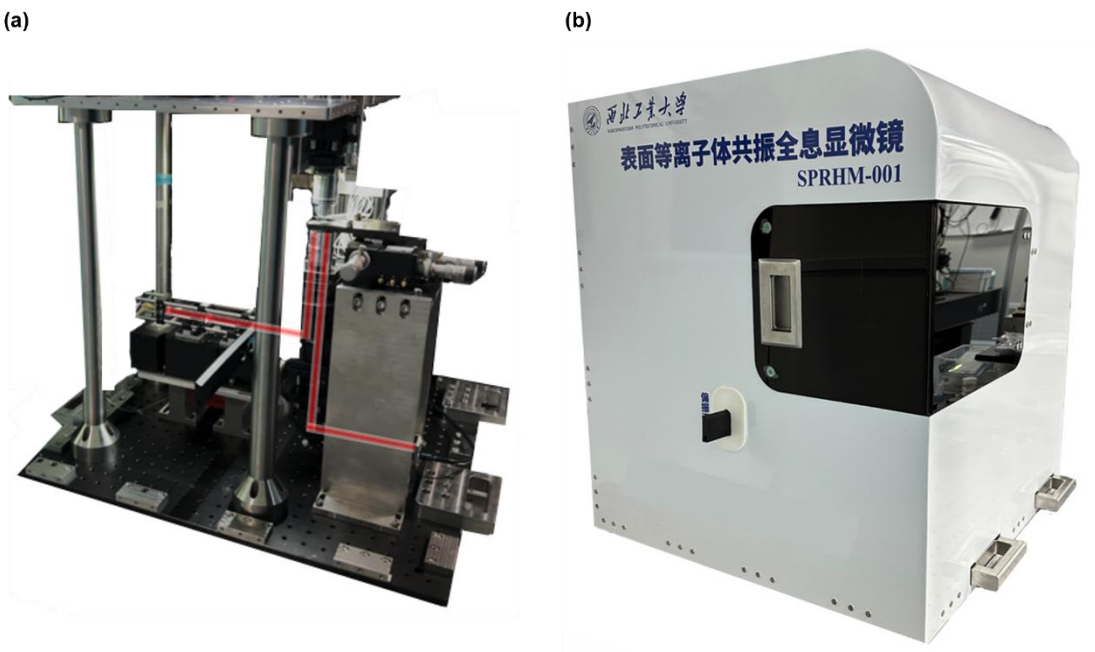

Figure S4 Assembly of the SPR holographic microscope. a Fabrication details of the internal opto-mechanical structure. All components are rigidly coupled to an optical breadboard with vibration-isolation tables. Red lines indicate the propagation path of the light beam. **b** External enclosure structure featuring hermetic seals at all interfaces.

Reference

1. Ma, C. J. et al. Lateral shearing common-path digital holographic microscopy based on a slightly trapezoid sagnac interferometer. *Optics Express* **25**, 13659-13667 (2017).